

Synthetic Positron Emission Tomography-Computed Tomography Images for Use in Perceptual Studies

Brian D'Alessandro^a, Mark Madsen^b, Ehsan Samei^c, Xiang Li^c, Jin Wooi-Tan^c, Kevin S. Berbaum^b, Kevin Scharz^b, Robert Caldwell^b, Lionel S. Zuckier^{a,*}

^a*Department of Nuclear Medicine, New Jersey Medical School, UMDNJ, Newark, NJ.*

^b*Department of Radiology, University of Iowa, Iowa City, IA.*

^c*Clinical Imaging Physics Group, Duke University Medical Center, Durham, NC.*

Abstract

To better understand fundamental issues, perception studies of the fusion display would best be performed with a panel of lesions of variable location, size, intensity, and background. There are compelling reasons to use synthetic images that contain artificial lesions for perception research. A consideration of how to obtain this panel of lesions is the nucleus of the present review. This article is a conjoint effort of 3 groups that have joined together to review results from work that they and others have performed. The techniques we review include (1) substitution of lesions into a preexisting image matrix (either using actual prior patient-derived lesions or mathematically modeled artificial lesions), (2) addition of images (either in the attenuation-corrected image space or at an earlier stage before image reconstruction), and (3) simulation of the entire patient image. A judicious combination of the techniques discussed in this review may represent the most efficient pathway of simulating statistically varied but realistic appearing lesions.

The perception of images remains a crucial issue in medical imaging, impacting upon a wide range of fundamental topics including training of readers, tools to enhance interpretation, design of equipment, ergonomics, and even medical liability. As medical technology is introduced at a rapid rate, there is an ongoing need to validate methods of medical imaging and image portrayal. American Food and Drug Administration (FDA) clearance to market a medical device requires demonstration that the device is substantially equivalent to a preexisting approved device; it does not mandate that the device be completely optimized for the task at hand. For this reason, devices may be introduced into the clinic without a complete understanding of the perceptual aspects of their use. This observation is true for equipment used in nuclear medicine as well as in other branches of medical imaging and display.

For example, many fundamental practices involved in the rendering of nuclear medicine images have not been thoroughly studied. Although the physical characteristics of positron emission tomography (PET) have been extensively investigated, substantially less work has been performed which focuses on observer perception of PET and PET-CT images. One question of interest is the adequacy of standard image fusion for the portrayal of pathology, a fundamental issue which impacts upon the optimal display of PET-CT and SPECT-CT images. Indeed, our data suggest that up to 20% of ¹⁸F-fluorodeoxyglucose (FDG)-

avid lesions, visible on PET alone, are not apparent on the fused images alone when using turn-key settings of a standard commercial workstation (Figure 1) [1].

Because of difficulties in controlling stimuli within images, perception research relating to medical imaging has generally been performed with simplified rather than actual clinical images [2,3]. Perception research is often directed at the investigation of situations believed to be prone to error, such as when clinical information is not available or multiple disease processes are present [4,5,6,7]. Trying to mimic these conditions in an experiment requires control over the presence and location of abnormalities. To better understand the fundamentals of this problem, perception studies of the fusion display would best be performed with a panel of lesions of variable location, size, intensity, and background. Performing observational studies with adequate statistical power requires a sufficient number of lesions with these appropriately varying characteristics. However, when employing actual clinical images as the test material, it is difficult to obtain a sufficient number of lesions with desired parameters, due to a generally low lesion frequency and the regulatory hurdles involved in using patient data. For this reason, use of synthetic images becomes an important strategy in obtaining sufficient cases for study. A consideration of how to obtain this panel of lesions is the nucleus of the present review. This article is a conjoint effort of three groups which have joined together to review results from work that they and others have performed. The techniques we review include (1) substitution of lesions into a preexisting image matrix

*Corresponding author, zuckier@yahoo.com

Seminars in Nuclear Medicine, vol. 41, no. 6, pp. 437-448, 2011
doi:10.1053/j.semnuclmed.2011.06.007

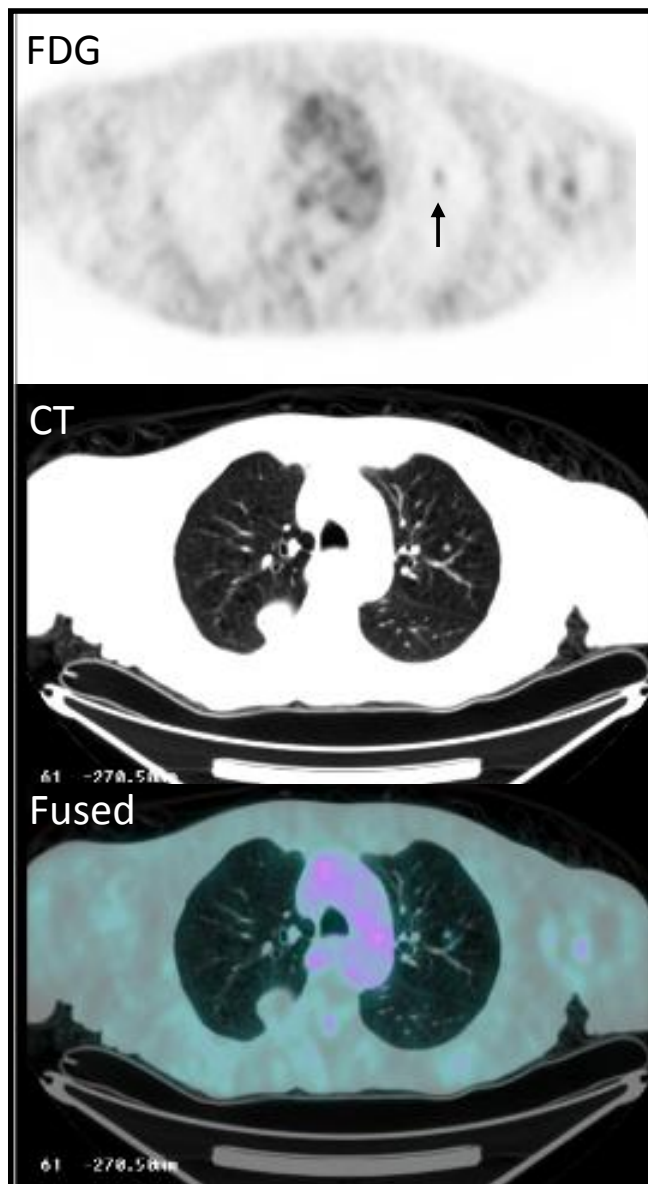


Figure 1: Loss of conspicuity of a FDG-avid lesion. A 65-year-old male with adenocarcinoma of distal esophagus is status post chemotherapy, radiation therapy and esophagectomy. A small FDG-avid nodule is seen in the left lung on FDG and CT images (arrow); however it is not discernable on the fused images obtained under default workstation settings.

(either using actual prior patient-derived lesions or mathematically modeled artificial lesions), (2) addition of images (either in the attenuation-corrected image space or at an earlier stage prior to image reconstruction), and (3) simulation of the entire patient image.

1. Image Matrix Substitution

1.1. Lesions obtained from a library of prior patient abnormalities

As an approach to the problem of generating synthetic images for perception research, investigators at the Uni-

versity of Iowa have developed a suite of software tools for mapping, removing, and inserting abnormalities into medical tomographic images. Their technique relies on manipulating images through removal of native lesions from abnormal images and insertion of non-native lesions into previously normal images. Initial work has focused on X-ray computed tomography (CT) of the thorax [8] while this review reports on expansion of the approach to include clinical whole body FDG-PET images. Observer experiments demonstrate that these images can be successfully manipulated without creating visual cues.

1.1.1. Technique

All of the software tools described in this section were developed using Interactive Data Language (IDL) and run as a compiled version on Windows-based computer systems that have the IDL Virtual Machine installed. The IDL Virtual Machine is freely available from ITT Visual Information Solutions. Three primary software tools were customized for PET imaging: Abnormality Mapping, Removal, and Insertion Tools.

The Abnormality Mapping Tool is used for viewing a PET study in the standard three orthogonal views in order to locate and potentially capture abnormal areas into libraries for future insertion into other selected PET studies. The coronal and sagittal views are generated from the axial slices with the vertical dimension appropriately adjusted for the inter-slice distance. The operator is able to use slider bars to adjust upper and lower display thresholds as well as to adjust the slice selection. In addition, each display area allows the operator to click on an image feature and the orthogonal views associated with the selected point are immediately redisplayed. By using this software, an operator can quickly review the PET study to find abnormal areas. When an abnormality is found, its location is logged with other pertinent information in a text file that is appended to each selected abnormality. Information from the log file can easily be imported into a spreadsheet application for further analysis or used as an input script file for the other software tools. Abnormalities of interest can also be selected for storage into a library file as they are logged by enabling a check box. A 64 x 64 area centered on the abnormality is copied into the next free entry space of a selected abnormality library. The operator has the option of selecting an existing library or creating a new library by clicking on the appropriate display buttons.

The PET abnormality removal tool follows the approach that was first developed for manipulating CT images [8]. Three dimensional ellipsoid image masks are used to remove an abnormality and replace it with a selected background area as shown in Figure 2. The operator finds the approximate centroid of the selected abnormality by adjusting the frame number and clicking on the abnormality. An elliptical region of interest is located at the centroid with the major and minor radii adjusted by the operator. The operator also adjusts the axial limits of the abnormality shown on the coronal and sagittal views

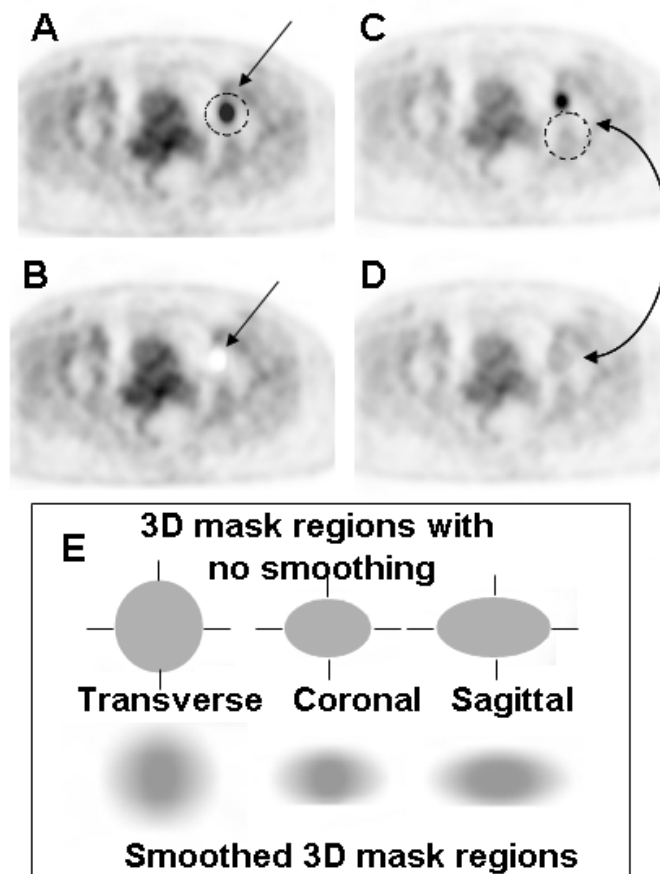


Figure 2: PET abnormality removal tool. A. An abnormal area is encompassed with an elliptical region of interest (arrow). B. An image mask associated with the region creates a void in the image. C. An offset replicate of the abnormality region is used to select a replacement area. D. The replaced area is added to the abnormality void. E. The region of interest is a volumetric ellipsoid where the operator controls the dimensions in the three orthogonal planes along with the degree of smoothing that is applied to the mask.

to generate the ellipsoid volume. On a separate display, an identical ellipsoid is also positioned by the operator to select an appropriate area in the background to use as a replacement for the abnormality. The complement of the mask (i.e., $1 - \text{mask}$) is multiplied into the image to create an ellipsoid void in the vicinity of the abnormality. The mask associated with the replacement area is multiplied into the image to get an ellipsoid image to replace the void. When these two are added together (with the appropriate location offsets), the abnormality is replaced; however, this creates an obvious boundary artifact at the ellipsoid edge. This problem is eliminated by adding a feature that smooths the ellipsoid mask using a boxcar average with an adjustable kernel width. This “feathers” the edges of both the void and the replacement data so that no edges are apparent. It should be noted that this operation does not cause any smoothing of the image. When the operator is satisfied with the removal, the images are updated with a mouse click. The revised study is saved with a new name when the operator moves on to the next study in the script.

The procedure for inserting abnormalities selected from libraries into other image sets is similar to the removal pro-

cess. The operator selects the starting frame and approximate location to insert an abnormality by clicking on the image, as shown in Figure 3. The sequential slices of the abnormality to be inserted are shown to the operator in a separate display. The operator uses a slider bar to select the abnormality entry from the library. An elliptical region is centered on the abnormality in each slice and the operator can change the major and minor radii to completely encompass the abnormality. The mask associated with the region is used to capture the abnormality. A separate set of 64×64 images of the area where the abnormality will be inserted is displayed below the abnormality set. These images are individual contiguous slices starting with the initially displayed slice. An identical but offset mask is used to create a void where the masked abnormality is inserted. As with the removal tool, the smoothing of the mask allows the abnormality to be inserted without edge effects. The location of the abnormality can be adjusted within these frames using x- and y-slider bars. In addition, there is another slider bar that allows the operator to adjust the intensity of the abnormality to better match the surrounding count density, or to alter its contrast. When the operator is satisfied with the location and appearance

of the abnormality, the study is updated and saved with a new file name. Examples of altered images are shown in Figure 4.

1.1.2. Validation

Physicians who routinely read imaging studies become expert in recognizing artifacts that the casual observer might not appreciate. In order to be certain that the removal and insertion tools do not leave visual cues that indicate alterations, observer experiments were performed. For the PET abnormality manipulation tools, the investigators recruited nine expert readers: five staff nuclear medicine physicians at the University of Iowa and the Iowa City VA Medical Center, three third-year nuclear medicine residents and one PET fellow. The observer experiment had 15 PET cases with abnormal areas removed and 15 PET cases with inserted library abnormalities. The cases were obtained from clinical PET whole body F-18 FDG images acquired at the University of Iowa Positron Emission Tomography Imaging Center with all patient identifiers removed.

For each case, all removal and insertion operations were performed on sequential axial images. From these altered axial images, whole body coronal planes were generated. Each case consisted of 10 contiguous coronal slices that encompassed the alteration. An additional unaltered study from a different patient also consisting of 10 contiguous coronal slices was displayed adjacent to the altered study (abnormality removal or insertion). The display location of the altered study (either right or left) was randomized. The display of the two image sets had one set of controls used for simultaneously scrolling through the individual images and for adjusting the upper and lower display thresholds.

The task of the observers was to identify which of the two displayed image sets had been altered. They had the ability to scroll through the displayed images and adjust display levels. The location of a suspected alteration was recorded with a mouse click. The observers also assigned a level of confidence to their selection ranging from 100% (absolute certainty) to 0% (best guess) in steps of 25%. There were no time constraints for finding the alterations and determining the level of confidence.

The performance of the observers for the 15 removal cases are presented in Table 1. Only one correct call was made for this portion of the evaluation and the observer assigned this the lowest confidence level (best guess). The results for the 15 insertion cases are presented in Table 2. Here the performance of the readers was better with a total of 15 correct calls (11%). The level of observer confidence for the insertion portion of the evaluation was significantly lower than for removals (53% vs. 39%). Also, there was no correlation between confidence level and correct calls. The performance of a consensus observer, representing the selections picked by the majority of observers, was also evaluated. The consensus observer had no correct calls.

Table 1: Results from Removal Cases

Observer	No. Correct (15 cases)	Mean Confidence Level
1	0	53%
2	0	31%
3	1	38%
4	0	66%
5	0	35%
6	0	65%
7	0	87%
8	0	63%
9	0	38%
Consensus*	0	53%

*Majority of observers with correct call.

Table 2: Results from Insertion Cases

Observer	No. Correct (15 cases)	Mean Confidence Level
1	1	28%
2	2	22%
3	3	28%
4	1	80%
5	3	33%
6	0	60%
7	2	63%
8	1	30%
9	2	8%
Consensus*	0	39%

*Majority of observers with correct call.

The results show that the removal and insertion software tools allow the manipulation of PET images without leaving obvious visual cues. Furthermore, the investigators believe the results indicate that these image manipulation tools can be used to create altered image sets for use in image perception studies. When appropriate care is used in applying these techniques, image sets can be altered without leaving visual cues that could potentially bias a perception experiment.

1.2. Lesions derived from mathematical modeling

The Iowa software tools enable insertion of lesions from a stored library of lesions into an unlimited number of normal patient studies. Nonetheless, because the library of lesions is extracted from real patient data, the number and range of lesions available may be constrained. Furthermore, the investigator must be very cautious in repeating use of an identical lesion in more than one test image. When a realistic-appearing lesion has been inserted into more than one image, the reader may learn to recognize the inserted lesion by virtue of the idiosyncratic pattern of noise within the abnormality. Therefore, there

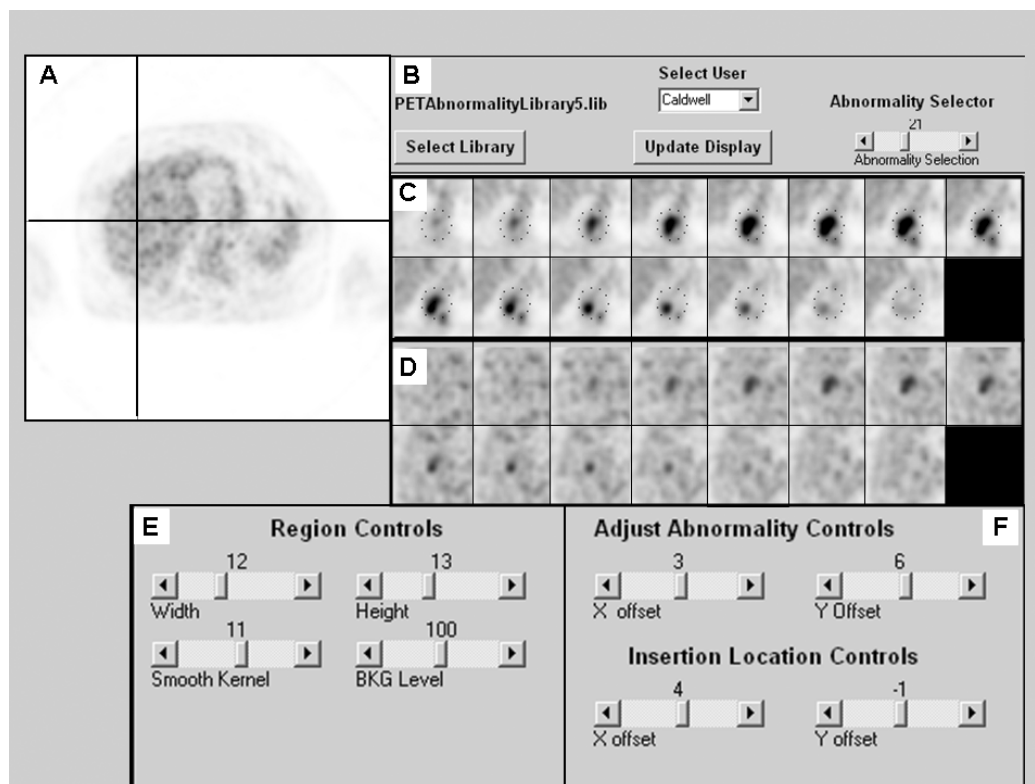


Figure 3: PET abnormality insertion tool. A. The operator selects the approximate location of the inserted abnormality (crosshairs). B. The abnormalities are located in library files where individual entries are selected with a slider bar. C. Sequential axial images of the selected library abnormality. An elliptical region is located on each slice of the abnormality. D. Sequential axial fragment images of the study where the abnormality will be inserted. A corresponding elliptical region creates a void where the mask selected abnormality will be inserted. E. Slider controls for adjusting the region parameters along with the mask smoothing and an adjustment for matching differences in count levels between the abnormality and the area where it is inserted. F. Controls for adjusting the location of the region of interest on the abnormality and for adjusting the insertion location.

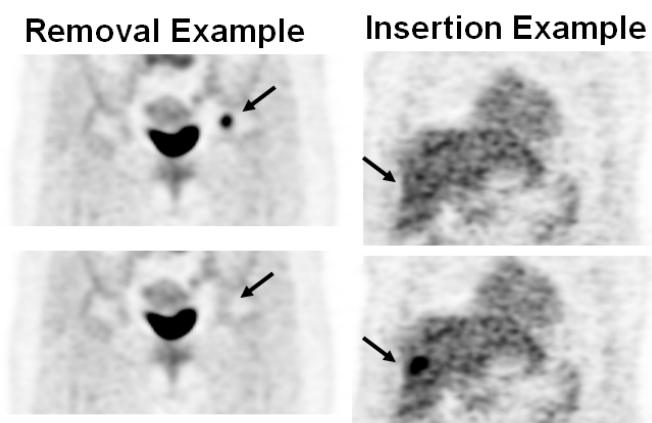


Figure 4: Examples of abnormality removal and insertion. The removal and insertion tools were applied on the axial slices. The coronal displays show slices through the altered volume.

is value in developing a method of producing lesions synthetically, which would not depend on their harvest from actual patient studies, and which could be repeated as many times as needed to generate a sufficient number of realistic-appearing discrete test cases.

In a method developed at Duke [9], mathematical mod-

eling of CT lesions was performed in order to create realistic-appearing simulated lesions. These lesions can presently be used to create the CT component of the PET-CT studies, and the technique has potential to be extended to create realistic FDG images as well. The method can essentially produce a large number of systematically-varied and

statistically-realistic lesions that can be inserted into actual patient images to create hybrid abnormal cases (i.e., images with real patient features and synthetic but realistic lesions).

1.2.1. Technique

In this method, three dimensional lung nodules are modeled as multiple 2-D masks on sequential CT slices. As CT has significantly higher spatial resolution than PET, replicating the true spatial features of the lesions are more demanding than PET lesion simulation. For a given 3-D nodule, its radii and peak contrasts on sequential CT slices can vary, depending on the vertical (z-direction) offsets of the nodule center relative to the CT slices (Figure 5). On each CT slice, the 2-D mask may be defined by a contrast profile equation proposed by Samei et al. [10] and reformulated by Burgess et al. [11] as

$$c(r) = C \left(1 - \left(\frac{r}{R} \right)^2 \right)^n \quad (1)$$

where R and C are the radius and peak contrast of the 2-D mask, and exponent n is a positive number inversely related to the steepness of the contrast profile, reflective of edge characteristics. Due to its radial symmetry, Equation (1) defines perfectly circular masks and has been adopted by Hoe et al. [12] to model small liver lesions on pediatric CT images.

To reflect the variability of real nodule shapes, radial asymmetry was introduced into Equation (1) by defining the radius as a function of polar angle, and the exponent as a function of radius, i.e.

$$\begin{aligned} c(r, \theta) &= C \left(1 - \left(\frac{r}{R_\theta} \right)^2 \right)^{n(R_\theta)} \\ n(R_\theta) &= n \frac{R_\theta}{R} \end{aligned} \quad (2)$$

where R_θ is a pre-defined nodule shape function, rescaled so that its average across all polar angles equals R , the nodule radius on the current CT slice obtained from initial geometric calculation. $n(R_\theta)$ was chosen as a linearly increasing function of R_θ to improve the smoothness of nodule border; the roughness induced by increasing nodule size from one polar angle to another is ameliorated by a corresponding decrease in the steepness of the nodule contrast profile. Because the steepness of the contrast profile of a spherical nodule can be shown to increase with the fraction of its diameter contained by a CT slice, f , a linear relationship was assumed between n and f as

$$n = \frac{n_{1/6} - n_1}{1/6 - 1} (f - 1) + n_1 \quad (3)$$

where n_1 and $n_{1/6}$ are exponents corresponding to conditions when all or one-sixth of the nodule diameter is contained by a CT slice, respectively.

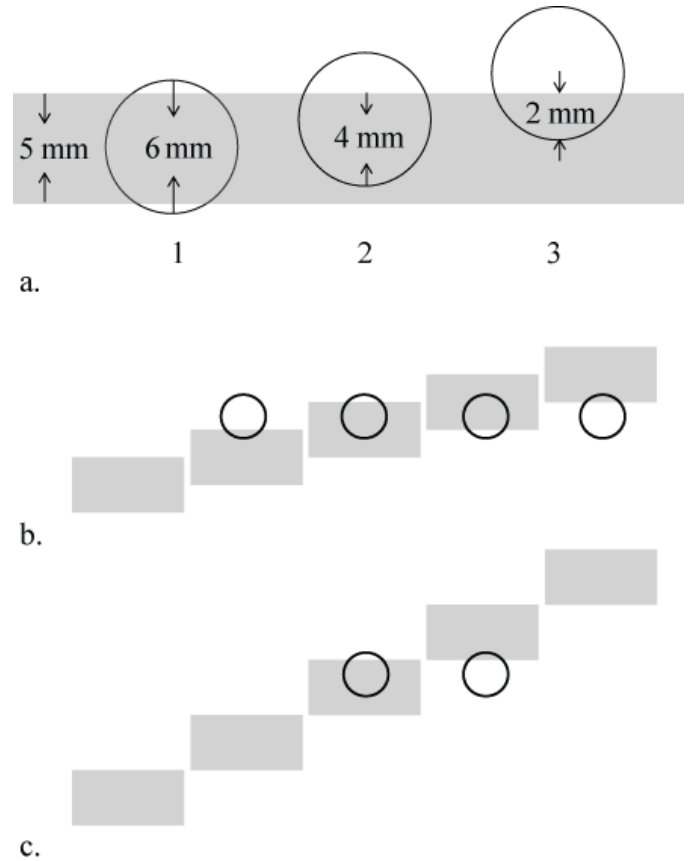


Figure 5: (A) For a 3-D nodule with diameter $2R_o$ of 6 mm, its radii on a 5-mm thick CT slice are 3, 3, and 2.83 mm for the vertical (z-direction) locations 1, 2, and 3, respectively. Assuming the peak contrast of the nodule to be proportional to its diameter subtended by the CT slice and defining its peak contrast at vertical location 1 as C_o , its peak contrasts at vertical locations 2 and 3 are $4C_o/5$ and $2C_o/5$, respectively. When changing the reconstruction interval from (B) half of the slice thickness, to (C) one slice thickness, the appearance of a nodule on contiguous CT slices also change.

To determine n_1 , Equation (1) was used to simulate spherical nodules fully enclosed by a CT slice with a sequence of n_1 values between 1.0 and 2.0. An experienced pediatric radiologist examined the nodule images and determined that n_1 values between 1.8 and 2.0 yielded the most realistic appearances. Subsequently, Equations (1) and (3) were used to create 3-D nodules visible on multiple contiguous CT slices with a sequence of $n_{1/6}$ values between 2.0 and 2.6 and an n_1 value of 2.0. The 3-D nodule images were examined by the same radiologist, who determined that $n_{1/6} = 2.4$ yielded the most realistic appearances. $n_1 = 2.0$ and $n_{1/6} = 2.4$ were used to calculate n in subsequent simulations.

Because shape variability contributes greatly to the difficulties associated with nodule detection, any realistic nodule simulation must reflect the variety of real nodule shapes. An algorithm was developed which generated a nodule shape function R_θ from 12 manually-specified base radii at evenly spaced polar angles with linearly interpolated values in between. A nodule shape function was first

designed for the central CT slice containing the nodule center. Slight variations were then added to four of the base radii, 90 degrees apart, to create nodule shape functions for the inferior and superior CT slices. Using this method, a library of 60 sets of nodule shape functions was created.

Lastly, to model nodules with diffused edges, a second component was added to Equation (2) as

$$c(r, \theta) = \alpha C \left(1 - \left(\frac{r}{R_{\theta}^{(1)}} \right)^2 \right)^{n(R_{\theta}^{(1)})} + (1 - \alpha) C \left(1 - \left(\frac{r}{R_{\theta}^{(2)}} \right)^2 \right)^{n(R_{\theta}^{(2)})} \quad (4)$$

where

$$\begin{aligned} n(R_{\theta}^{(1)}) &= n \frac{R_{\theta}^{(1)}}{R^{(1)}} \\ n(R_{\theta}^{(2)}) &= \left(\frac{n}{\gamma} \right) \frac{R_{\theta}^{(2)}}{R^{(2)}} \\ R^{(1)} &= \frac{R}{\beta} \\ R^{(2)} &= R \end{aligned} \quad (5)$$

Here, $R_{\theta}^{(1)}$ and $R_{\theta}^{(2)}$ are two nodule shape functions, rescaled so that their averages equal $R^{(1)}$ and $R^{(2)}$, respectively. Peak contrast C is shared between the two components in an $\alpha : (1 - \alpha)$ ratio. Relative to the first component, the exponent of the second component is reduced by γ fold, while the average radius of the second component is increased by β fold. Both C and n were derived from the radius of the first component, $R^{(1)}$. Simulations were performed for sequences of α , β , and γ over the ranges of 0.2-0.8, 1.1-1.5, and 0.5-1.6, respectively. Values of $\alpha = 0.4$, $\beta = 1.3 - 1.4$, and $\gamma = 1.3$ provided the most realistic nodule appearances. Equations (4) and (5) with $\alpha = 0.4$, $\beta = 1.4$, and $\gamma = 1.3$ were subsequently used to create double-component nodules, each of which adopted two sets of nodule shape functions, randomly sampled from the library. Sixty pairs of function sets were selected by an experienced pediatric radiologist and added to the library, bringing the total number of designs to 120 (i.e. 60 single-component and 60 double-component designs). Figures 6 and 7 illustrate examples of real and simulated nodules on pediatric chest CT images.

1.2.2. Validation

CT images of 34 real nodules and 55 simulated nodules were randomized and rated independently by four experienced pediatric radiologists on a continuous scale of appearance between 0 (definitely not real) and 100 (definitely real). Receiver operating characteristic (ROC) analysis, t-test, and equivalence test were performed to assess the radiologists' ability to distinguish between simulated and

real nodules. The areas under the ROC curves were 0.59, 0.60, 0.40, and 0.63 for the four observers. Mean score differences between simulated and real nodules were -8, -11, 13, and -4 for the four observers with p-values of 0.17, 0.06, 0.17, and 0.26, respectively. The results of the observer study showed that the simulated and real nodules were perceptually indistinguishable to experienced observers.

The method described above for creating asymmetric 2-D nodule masks in CT has been successfully used for simulating lung and liver lesions, and has been adapted to create lung nodules on chest radiographs. Mathematical modeling of lesions can be applied for simulation of PET-CT images, both for creation of the CT component, and, with modification based on the particulars of the FDG images, for the PET component as well.

1.3. Methods of Image Addition

1.3.1. Summation of attenuation-corrected images

An easy and straightforward method of creating PET images with synthetic lesions is by summing suitable attenuation corrected (AC) PET images of lesions and patient background. Advantage of the image addition methods, in contrast to matrix substitution techniques, is that they obviate the need to match background intensities and blend edges of inserted regions of the image. A limitation of the image addition techniques is that they do not lend themselves to creating lesions which may have pixels with intensities less than the original image, as may occur clinically in regions of necrosis.

In this method, AC images of artificial lesions, imaged within a waterbath devoid of activity and modeled to represent desired distributions of activity, are filtered to reduce high-frequency detail and then arithmetically added to normal AC patient image matrices to create summation images. At their simplest, these lesions consist of hollow spheres which can be inserted into a waterbath. The spheres are filled with predetermined concentrations of ^{18}F -FDG and are surrounded by water devoid of activity. By imaging radioactive clay or wax composition models [13], a similar process could be used to create non-homogenous lesions that mimic virtually any desired morphological or anatomical characteristic.

Because image acquisition and processing are non-linear, it was found that artificially inserted balls had slightly sharper edge characteristics than what was present in true images [14]. To reduce the effect of edge artifacts, a filtering step must be performed on the artificial lesion prior to background embedding. Two methods are being investigated for filtering: wavelet packet decomposition [15], and simple low-pass filtering [16]. Preliminary studies at the New Jersey Medical School, performed using a Jaszczak phantom where synthetic images can be compared to actual images of the simulated composition, have been performed to estimate the appropriate cutoff frequency needed for this low-pass filter (Figure 8), which will be further tested through forced choice validation.

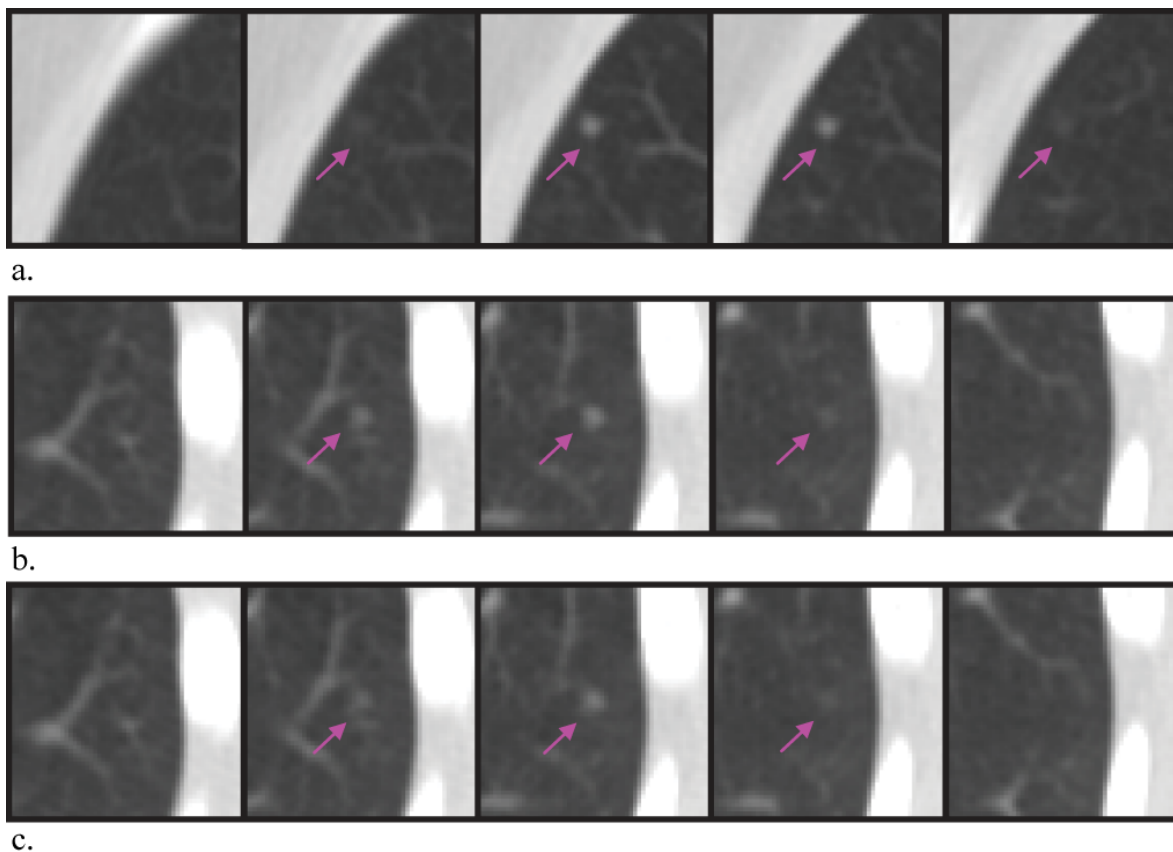


Figure 6: (a) An example real nodule visible on multiple contiguous transverse CT slices. (b) An example simulated single-component nodule. (c) An example simulated double-component nodule. Both simulated nodules are also visible on multiple contiguous transverse CT slices. All regions of interest are 30 mm in size.

1.3.2. Summation of pre-reconstruction data

To simulate images where hot lesions are embedded within organs, the group at the University of Pennsylvania has also used a method where data from a separately imaged artificial hot lesion (imaged without background) are added to data from a patient study without pathology [17,18,19]. However, to achieve a realistic appearance, the raw patient background and artificial lesion data are combined together prior to reconstruction of the combined data, thereby preserving the statistical accuracy of the raw data. Early work in this direction was performed using data in sinogram format followed by reconstruction [18], while the recent technique involves merging data in list-mode followed by an iterative list-mode reconstruction [17,19]. The format of the raw data (sinogram versus list-mode) used in reconstruction requires different techniques to realistically merge the patient and artificial lesion data set.

In a validation study [17], list mode data were acquired of a cylindrical tank filled with an ^{18}F -FDG solution (the background), and of ^{18}F -FDG -filled plastic spheres suspended in air (the lesions). Images were also acquired of the spheres submerged in the tank for the “true” case comparison. The spherical lesion in air data were first attenuated according to the transmission map of the background

activity. Next, an appropriate number of events from the lesion acquisition were randomly mixed into the event list of the background in order to achieve a pre-defined lesion uptake relative to the background. This merged list was then reconstructed with all appropriate corrections to form the final visible images. Validation of this fusion procedure was performed by a comparison of the histogram, background pixel noise, and sphere-to-background contrast between the fused images and the true images, for which the results agree well. The authors also demonstrate use of this method to embed the artificial spherical lesions into a background of actual patient data [17,19] (Figure 9).

This approach provides a powerful method of combining artificial lesions with actual patient images in a highly-realistic manner. More irregular distributions of activity could be created and imaged using radioactive clay or wax, as mentioned above [13]. The strength of this method is in the fact that introduction of the artificial lesions into the patient data avoids problems with the summation of images after non-linear reconstruction. However, the method is relatively technically demanding as it requires access to and manipulation of raw data, interventions which are usually not accessible to system users. Nonetheless, it represents a gold standard in terms of lesion fidelity in the context of actual patient images.

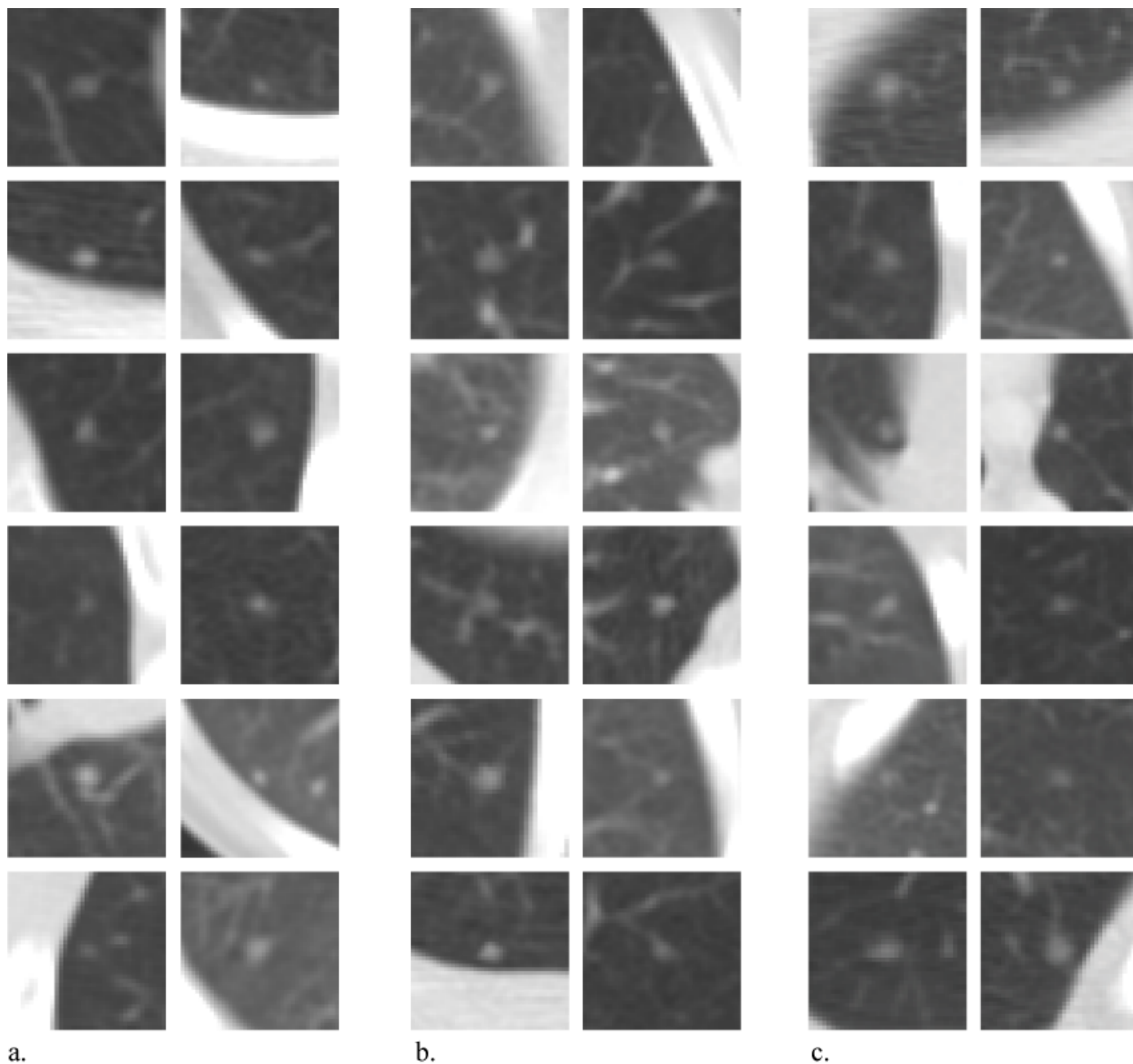


Figure 7: Examples of real and simulated 2-D nodule masks, showing the varieties of nodule shape, contrast, and marginal characteristics. The nodule masks have diameters of 2.5-6 mm and are located at the centers of the regions of interest. (a) Real nodule masks. (b) Simulated single-component nodule masks. (c) Simulated double-component nodule masks.

1.4. Lesions within a simulated patient

A comprehensive method of simulating both the lesion and the surrounding tissue can be performed using the method of Segars and Tsui et al. [20,21,22]. Computer simulations have been limited by the accuracy of the simulation tools and the level of detail which is programmed into the simulation. Recent advances have been made in the anatomical modeling of the human body as well as in the sophistication of Monte Carlo methods. The latter can be used to model the complex imaging system and physics of the imaging process to simulate medical imaging over

a wide variety of modalities (such as SPECT, PET, MRI and CT). In particular, the 4-D Extended Cardiac-Torso (XCAT) Phantom features a high level of realism in its human body model [20,21,22]. Over 9000 anatomical objects are defined in the phantom, including brain structures, interior detail of the breast, blood vessels, and muscles of the heart. Each object was modeled using 3D software from the segmentation of high-resolution anatomical slice datasets, MRI data, or CT data. Object models were defined using a combination of nonuniform rational B-splines (NURBS) and subdivision surfaces, which efficiently pa-

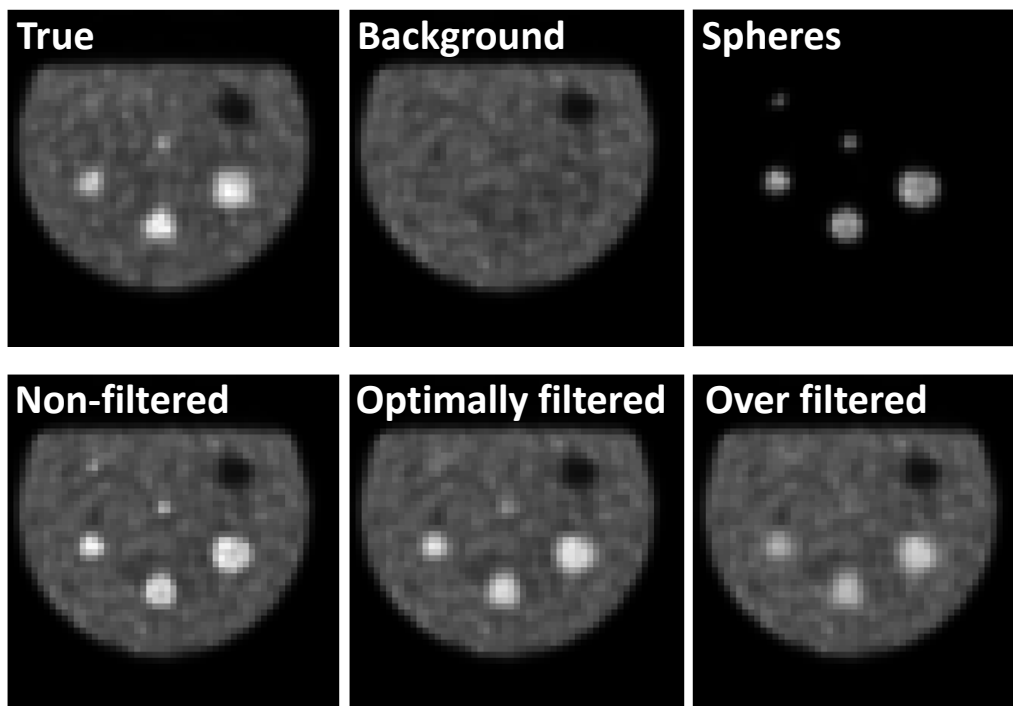


Figure 8: Example of summed AC images. Concentration of activity in the background, balls alone, and balls within background is equivalent to SUV values of 2, 4 and 6 respectively. Optimal lesion filtering was obtained using a Hamming-window based, linear-phase low-pass filter of length 10, with a normalized cutoff frequency of 0.5. The over-filtered lesions were obtained using a normalized cutoff frequency of 0.3. Note effect of filtering on the smallest spheres located centrally, and at the 10 o'clock position.

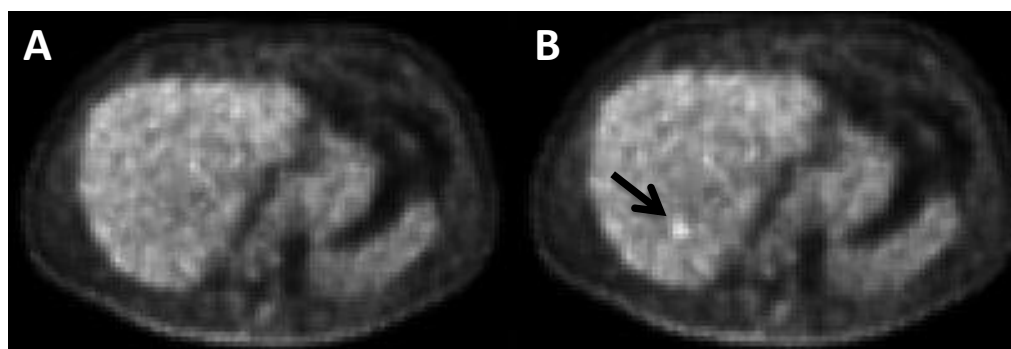


Figure 9: Example of summation of list-mode data to introduce artificial lesions into a normal patient's scan (arrow). Modified from reference [19] and reproduced with permission.

parameterize and smooth the 3D object surface meshes. The XCAT phantom not only models anatomical objects in 3D, but also movement over time, such as breathing motion based on respiratory gated CT images and the motion of a beating heart based on tagged MRI images. This full 4D representation allows a high level of realism in simulating medical imaging processes to obtain virtual imaging data which are comparable to the true imaging process.

With this type of simulation, it is possible to model a lesion anywhere inside any organ in the body to obtain simulated PET images. Lesion size, shape, location, and the distribution of radiopharmaceutical within the organ, based on known pathophysiology, can be precisely stipu-

lated. With full body simulation, incorporating thousands of anatomical objects acquired under specified clinical and imaging conditions, investigators can study a wide variety of parameters which affect perception at an accuracy and realism comparable to true PET imaging of actual patients. Future progress in modeling and computer processing will further advance the realism and practicality of this technique.

Investigation has currently been conducted using this method to evaluate the effect of respiratory motion on lung and liver lesion detection in oncological PET, and to assess the results of PET motion compensation techniques (Figure 10) [23,24,25]. The method has also been used to sim-

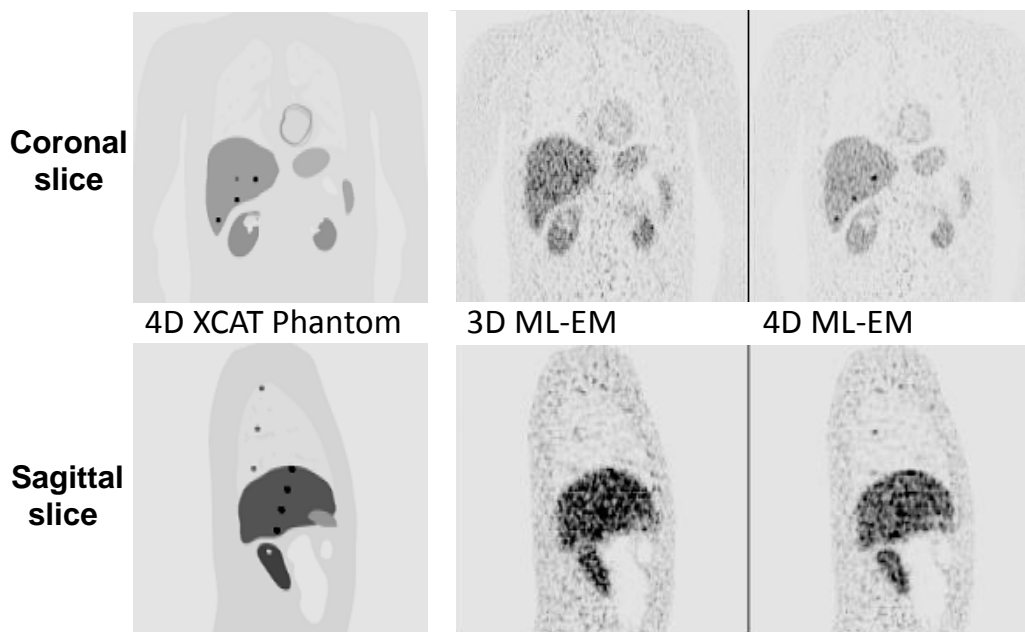


Figure 10: Representative coronal (top row) and sagittal (bottom row) images demonstrate reconstructed PET images without (second column) and with (third column) motion compensation of the simulated projection data. Theoretical distribution of activity in the 4D XCAT Phantom (ground truth) is illustrated in the images in the first column. Note variable appearance of simulated lesions within the lung and liver. Images courtesy of S. Chen and B. Tsui [24,25].

ulate detection of defects in myocardial perfusion SPECT and would be equally applicable to cardiac PET [26,27,28]. By realistically modeling the coronary arterial tree for the heart model of the XCAT phantom, a myocardial perfusion defect can be generated by simulating a stenotic lesion at a specific location of the coronary arterial tree, resulting in a perfusion lesion of realistic extent and shape. With the flexibility to introduce lesions of a given composition at any location within the body, this method has potential for simulating virtually any clinical condition that is subject to modeling based on an understanding of the distribution of radiopharmaceutical for the given disease state.

2. Conclusion

There are compelling reasons to use synthetic images that contain artificial lesions for perception research. Techniques used to create these images should have the capacity to generate a large number of lesions of variable size and intensity, produce stochastically unique lesions, and exhibit ease and universality of implementation. An additional desirable feature of these techniques would be the ability to relate artificial lesions to the underlying pathology at the tissue activity concentration level, which would allow the perceptual task to be related to a ground truth within the simulated patient. In hybrid imaging, there must also be a method of correlating artificial lesions generated within the multiple modalities. A judicious combination of the techniques discussed in this review may represent the most

efficient pathway of simulating statistically varied but realistic appearing lesions.

3. Acknowledgments

The authors would like to thank Dr. Benjamin M. W. Tsui, Dr. Suleman Surti, and Dr. Joel S. Karp for their helpful feedback and assistance in providing some of the figures.

References

1. Zuckier LS, Ghesani NV, Liu Y (2007) Perspicuity of solitary oncologic lesions on fused 18F-FDG PET-CT images. Society of Nuclear Medicine 54th Annual Meeting. Washington DC. pp. 377P.
2. Abbey CK, Eckstein MP (2007) Classification images for simple detection and discrimination tasks in correlated noise. *J Opt Soc Am A Opt Image Sci Vis* 24: B110-124.
3. Abbey CK, Pham BT, Shimozaki SS, Eckstein MP (2008) Contrast and stimulus information effects in rapid learning of a visual task. *J Vis* 8: 8 1-14.
4. Berbaum K, Franken EA, Jr., Caldwell RT, Schartz KM (2006) Can a checklist reduce SOS errors in chest radiography? *Acad Radiol* 13: 296-304.
5. Berbaum KS, El-Khoury GY, Ohashi K, Schartz KM, Caldwell RT, et al. (2007) Satisfaction of search in multitrauma patients: severity of detected fractures. *Acad Radiol* 14: 711-722.

6. Berbaum KS, Franken EA, Jr., Dorfman DD, Caldwell RT, Lu CH (2005) Can order of report prevent satisfaction of search in abdominal contrast studies? *Acad Radiol* 12: 74-84.
7. Krupinski EA, Berbaum KS (2009) The medical image perception society update on key issues for image perception research. *Radiology* 253: 230-233.
8. Madsen MT, Berbaum KS, Ellingson AN, Thompson BH, Mullan BF, et al. (2006) A new software tool for removing, storing, and adding abnormalities to medical images for perception research studies. *Acad Radiol* 13: 305-312.
9. Li X, Samei E, Delong DM, Jones RP, Gaca AM, et al. (2009) Three-dimensional simulation of lung nodules for paediatric multidetector array CT. *Br J Radiol* 82: 401-411.
10. Samei E, Flynn MJ, Eyer WR (1997) Simulation of subtle lung nodules in projection chest radiography. *Radiology* 202: 117-124.
11. Burgess AE, Li X, Abbey CK. Nodule detection in two component noise: toward patient structure. In: Kundel HL, editor 1997 February 26; Newport Beach, CA, USA; Bellingham, Wash: International Society for Optical Engineering, 1997.
12. Hoe CL, Samei E, Frush DP, Delong DM (2006) Simulation of liver lesions for pediatric CT. *Radiology* 238: 699-705.
13. Turkington TG, Degrado TR, Sampson WH. Small spheres for lesion detection phantoms; 2001 2001. pp. 2234-2237.
14. Zuckier L, Zanzonico P, Patel VB (2008) Synthetic FDG PET Hepatic Lesions for Evaluation of Image Display and Perception (oral). *RSNA 2008*. Chicago, IL. pp. 592.
15. Mallat S (1999) *A Wavelet Tour of Signal Processing*: Academic Press.
16. Gonzalez RC, Woods RE (2008) *Digital Image Processing*: Pearson Prentice Hall. - p.
17. El Fakhri G*, Surti S*, Trott CM, Scheuermann J, Karp JS (2011) Improvement in Lesion Detection with Whole-Body Oncologic Time-of-Flight PET. *J Nucl Med* 52: 347-353. (* joint first authors).
18. El Fakhri G, Santos PA, Badawi RD, Holdsworth CH, Van Den Abbeele AD, et al. (2007) Impact of Acquisition Geometry, Image Processing, and Patient Size on Lesion Detection in Whole-Body 18F-FDG PET. *J Nucl Med* 48: 1951-1960.
19. Surti S, Scheuermann J, El Fakhri G, Daube-Witherspoon ME, Lim R, et al. (2011) Impact of time-of-flight PET on whole-body oncologic studies: a human observer lesion detection and localization study. *J Nucl Med* 52: 712-719.
20. Segars WP, Mahesh M, Beck TJ, Frey EC, Tsui BMW (2008) Realistic CT simulation using the 4D XCAT phantom. *Medical Physics* 35: 3800-3808.
21. Segars WP, Sturgeon G, Mendonca S, Grimes J, Tsui BMW (2010) 4D XCAT phantom for multimodality imaging research. *Medical Physics* 37: 4902-4915.
22. Segars WP, Tsui BMW (2009) MCAT to XCAT: The evolution of 4-D computerized phantoms for imaging research. *Proceedings of the IEEE* 97: 1954-1968.
23. Rahmim A, Dinelle K, Cheng JC, Shilov MA, Segars WP, et al. (2008) Accurate event-driven motion compensation in high-resolution PET incorporating scattered and random events. *IEEE Transactions on Medical Imaging* 27: 1018-1033.
24. Chen S, Tsui B. Four-Dimensional OS-EM PET Image Reconstruction Method with Motion Compensation; 2009 September 5-10, 2009; Beijing, China. pp. 373-376.
25. Chen S (2011) *Development of 4D Image Reconstruction Method with Respiratory Motion Compensation for Oncological PET Imaging*. Baltimore, MD: Johns Hopkins University.
26. Yang YW, Chen JC, He X, Wang SJ, Tsui BMW (2009) Evaluation of respiratory motion effect on defect detection in myocardial perfusion SPECT: A simulation study. *IEEE Transactions on Nuclear Science* 56: 671-676.
27. Fung GSK, Lee TS, Higuchi T, Tsui BMW, Segars WP, et al. Realistic simulation of regional myocardial perfusion defects for cardiac SPECT studies; 2010 Oct. 30 2010-Nov. 6 2010 Knoxville, TN, USA IEEE. pp. 3061-3064.
28. Fung GSK, Segars WP, Veress AI, Gullberg GT, Tsui BMW. Toward modeling of regional myocardial ischemia and infarction: generation of realistic coronary arterial tree for the heart model of the XCAT phantom; 2009 8 February 2009; Lake Buena Vista, FL, USA. pp. 726215.